Materials & Design 244 (2024) 113225

Contents lists available at ScienceDirect

Materials & Design

journal homepage: www.elsevier.com/locate/matdes

Compressive residual stress applied to a low-carbon steel surface alloyed with WC tool constituent elements according to friction stir processing

Hajime Yamamoto *, Yuji Yamamoto, Kazuhiro Ito, Yoshiki Mikami

Joining and Welding Research Institute, Osaka University, 11-1 Mihogaoka, Ibaraki, Osaka 567-0047, Japan

ARTICLE INFO

Keywords:
Friction stir processing
Residual stress
Surface alloying
Retained austenite
Deformation-induced martensitic transformation
Tungsten carbide

ABSTRACT

Friction stir processing (FSP) effectively improves the fatigue strength of arc-welded joints; however, wear of tools is inevitable in case of high-strength materials. Notably, a new benefit has been discovered: compressive residual stress is applied on the FSPed steel surface, alloyed with the WC tool constituent elements, contrasting with the tensile residual stress typically applied via conventional FSP. To elucidate the mechanism of compressive residual stress application, FSP was performed on a low-carbon steel plate at various rotational speeds. The alloyed topmost layers in the stir zone comprised martensite structures with a small amount of retained austenite grains, resulting in a hardness increase owing to the tool constituent elements. The residual stresses on the stir zone surface were influenced by the alloying contents and the corresponding martensite start temperature (Ms). Compressive residual stresses were maximized at an Ms of approximately 150 °C owing to martensitic transformation expansion near room temperature. Lowering the Ms below approximately 150 °C led to tensile residual stresses and an increased volume fraction of the retained austenite, suggesting that martensitic transformation expansion is insufficient to apply compressive residual stress. Conversely, the retained austenite can resist plastic deformation and crack propagation through deformation-induced martensitic transformation, thereby enhancing fatigue properties.

1. Introduction

The fatigue strength of arc-welded joints is lower than that of the base metal owing to stress concentration, tensile residual stress, and microstructural deterioration at the weld toe. Various post-weld treatments have been proposed to leverage high-strength materials in welded structures. Typical treatments include residual stress modification, such as peening [1,2] and post-weld heat treatment [3,4], and weld geometry modification, such as grinding [5,6] and remelting [7,8]. Residual stress modification improves fatigue strength at low-stress amplitudes but is less effective at high-stress amplitudes owing to residual stress relaxation caused by plastic deformation during fatigue. Conversely, weld geometry modification can be effective at any stress level. However, grinding requires skilled technicians, is time-consuming, and reduces weld thickness. Remelting with arc plasma or laser as a heat source also has the drawback of softening around the remelted zone in high-strength materials.

Furthermore, we reported that friction stir processing (FSP) considerably increased the fatigue strength of arc-welded steel joints, presenting it as a new post-weld treatment [9–11]. Generally, FSP, based on the principle of friction stir welding (FSW), is a surface modification technique that homogenizes and refines the microstructure of various metallic materials in a solid state [12]. The mechanical properties of the stir zone, such as strength, ductility, and fracture toughness, can surpass those of the base metal [13–17]. In addition, material flow around the rotating tool during FSP helps eliminate internal defects such as porosity, segregation, and cracks caused by melting and solidification, thereby enhancing the fatigue properties of casts [18–20] and additively manufactured components [21–24]. Leveraging these advantages, Costa et al. reported that performing FSP on the weld toes improved the fatigue strength of arc-welded aluminum alloy joints [25–28].

Although FSP offers several advantages over conventional methods, tool wear remains is inevitable in case of high-strength materials owing to the high temperatures and pressures required for FSP. In our previous studies [10,11], the wear of a WC tool tip during FSP was found to have a beneficial application on the weld toes of arc-welded steel joints. The tool constituent elements were alloyed with the topmost layer of the stir zone, resulting in an unexpected new benefit depending on the alloying

* Corresponding author.
E-mail address: yamamoto.hajime.jwri@osaka-u.ac.jp (H. Yamamoto).

https://doi.org/10.1016/j.matdes.2024.113225
Received 13 June 2024; Received in revised form 16 July 2024; Accepted 31 July 2024
Available online 2 August 2024

contents—the generation of compressive residual stress. The alloying mechanism related to tool wear in the low-carbon steel plate was investigated using a stop-action technique to observe the tool/steel interface during FSP [29]. As the tool rotational speed increased, Fe atoms diffused from the steel side into the Ni-based binder regions of the tool. Some WC particles reacted with Fe atoms to form a brittle Fe_4W_2C layer at the tool/steel interface. This Fe_4W_2C layer was fragmented and decomposed by shear stress and frictional heat during FSP, resulting in the alloying of W and C into the steel matrix. This study is the first to explain the mechanism of compressive residual stress application to the topmost layer alloyed with the tool constituent elements, despite conventional FSP and FSW typically generating tensile residual stresses owing to thermal and mechanical strains on the stir zone surface [30–33].

In this study, FSP, accompanied by alloying with WC tool constituent elements at various tool rotational speeds, was conducted on a low-carbon steel plate. The effects of alloying contents on the microstructure formation of the stir zone were investigated to elucidate the mechanism of compressive residual stress application to the topmost layer. The mechanical properties of the alloyed topmost layer were also characterized.

2. Experimental procedures

In our previous studies [10,11], FSP with a spherical-tip tool was conducted on steel weld toes with curved surfaces, but the metallurgical and mechanical phenomena were complicated by the geometric effect. Therefore, this study simplified the FSP conditions using a flat steel plate and a flat-tip tool to focus mainly on the residual stress analysis. SM490A low-carbon steel plates (Fe–0.16C–0.29Si–1.37Mn–0.008P–0.001S (mass%)) with dimensions of 150 mm × 50 mm × 10 mm were used as the base material. The steel plates exhibited a ferrite–pearlite structure. FSP was performed on the steel plate. The tool, featuring a 15-mm-diameter flat tip, was made of WC particles (88–91 mass%) and a Ni-based binder. The tool was tilted backward at 3° and operated at a travel speed of 100 mm/min and a plunge depth of 0.8 mm, with rotational speeds of 600, 800, and 1000 rpm. The right and left positions along the FSP direction are referred to as the advancing side (AS) and retreating side (RS), respectively, based on the tool's counterclockwise rotation.

Specimens were taken from the FSPed steel plate for microstructure evaluations, residual stress measurements, and mechanical tests. The shapes, dimensions, and positions of the specimens taken from the FSPed steel plate are shown in Fig. 1.

Cross-sectional microstructure observations of the FSPed steel plates were conducted via optical microscopy (OM) and scanning electron microscopy (SEM) coupled with electron backscatter diffraction (EBSD). Elemental concentration distributions in the topmost layer of the FSPed steel plates were analyzed via electron probe microanalysis (EPMA). The cross-sections were polished with colloidal silica for EBSD and EPMA. Vickers hardness tests were performed on the OM observation areas at room temperature with an applied load of 98 mN and a loading time of 10 s.

Residual stresses on the FSPed steel surface were measured via the $\sin^2\psi$ technique using a micro-X-ray diffractometer (μ-XRD) employing Co-Kα radiation. X-rays passing through a collimator with a diameter of 0.8 mm were irradiated on the FSPed steel surface for 2 min at 5° intervals in the ψ angle range of 45°–90°, and the $\{220\}_{\alpha\text{-Fe}}$ diffraction peaks were collected on an area detector. The FSPed steel plate fixed on a movable stage was tilted at the ψ angle with respect to the axes parallel and perpendicular to the FSP direction, obtaining the residual stresses in each direction. The volume fraction of the retained austenite (γ) on the FSPed steel surface was estimated using the same μ-XRD based on the integrated intensities of diffraction peaks collected over 75 min in the diffraction angle range of 23.3°–116.7°, according to ASTM E975-22 [34].

Small tensile specimens with a dumbbell shape were taken from the topmost layer of the FSPed steel plate. Tensile tests were conducted at room temperature with a nominal strain rate of 2.5×10^{-4} s^{-1}. The tensile direction was perpendicular to the FSP direction. Local strain and volume fraction of the retained γ on the specimen surfaces were measured four times at nominal strains of 0 % (before testing), 3 %, 5 %, and 7 % (fractured). For comparison, a specimen subjected to sub-zero treatment in liquid nitrogen for approximately 1 h was also tested to investigate the effect of the volume fraction of the retained γ on tensile properties.

A compact tension (CT) specimen with a thickness of 1.3 mm was taken from the surface of the FSPed steel plate. Fatigue crack propagation tests were performed at room temperature, applying cyclic loads at

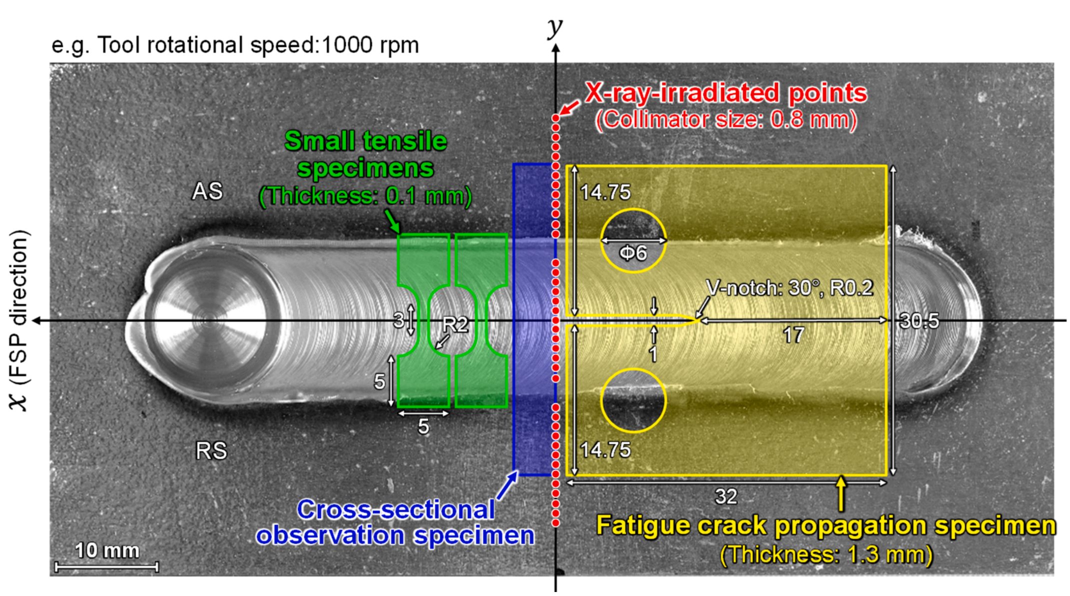

Fig. 1. Shapes and dimensions of specimens used for cross-sectional observation (blue), tensile testing (green), and fatigue crack propagation testing (yellow), and their positions on the FSPed steel plate (e.g., at a tool rotational speed of 1000 rpm). X-ray-irradiated points, indicated in red, were used to measure the volume fraction of the retained γ and residual stress before cutting. (For interpretation of the references to colour in this figure legend, the reader is referred to the web version of this article.)

a stress ratio of 0.1 (minimum and maximum loads of approximately 48.9 and 488 N, respectively) with a sinusoidal wave frequency of 20 Hz. The change in crack length during testing was sequentially measured using the compliance method with a strain gauge attached to the back surface of the specimen, and the crack propagation rate was determined for each stress intensity factor range. The fatigue fracture surfaces after testing were observed via SEM.

3. Results and discussion

3.1. Microstructure in the FSPed steel surface alloyed with tool constituent elements

The elemental concentration distributions were analyzed via EPMA to investigate the distribution of tool constituent elements in the stir zone of the FSPed steel plates. Backscattered electron (BSE) images and EPMA-W maps of the cross-sections of the stir zone at rotational speeds of 600, 800, and 1000 rpm are shown in Fig. 2. The stir zones, indicated by the regions above the broken lines in Fig. 2(a)–(f), had a depth that increased slightly with increasing tool rotational speed. W-rich layers were observed across the entire width of the stir zone surface, and their W contents in the topmost areas were slightly increased from the center to the AS. The overall average W contents were estimated to be approximately 1.5, 6.0, and 9.0 mass% at 600, 800, and 1000 rpm, respectively. The layer formed at 1000 rpm displayed the greatest thickness and content among those formed at the aforementioned three rotational speeds (Fig. 2(i)). Similarly, other tool constituent elements, such as C and Ni, were distributed at the same positions at each rotational speed. The discontinuity of the alloyed layer at lower rotational speed may be caused by weak material flow with a mixture of worn and unworn areas in the contact surface of the tool tip (Fig. 2(g) and (h)). As the rotational speed increases, the relatively uniform and thick alloyed layer can be formed by the strong material flow with the wear occurring in the whole contact surface of the tool tip (Fig. 2(i)).

The effects of alloying tool constituent elements on the microstructure formation in the stir zone were investigated using EBSD. The EBSD-inverse pole figure (IPF) and phase maps obtained from the white rectangular areas in Fig. 2(g)–(i) are shown in Fig. 3, with the alloyed areas identified by EPMA depicted by white broken lines. The stir zone consisted of lath martensite (α') under all FSP conditions (Fig. 3(a), (c), and (e)). It is believed that the initial ferrite–pearlite structure fully transformed to the γ phase at elevated temperatures during FSP. Tool constituent elements such as W and C dissolved into the γ phase in the topmost layer near the tool tip, followed by α' transformation during cooling. The α' lath width in the alloyed layers was considerably smaller than in the non-alloyed regions, indicating that the alloying elements suppressed grain growth. The grain size of the alloyed layer did not show the monotonous change with increasing tool rotational speed, because both the alloying contents and the peak temperature during FSP increased simultaneously. In addition, the alloyed layers exhibited the FCC phase, shown in green in the EBSD-phase maps (Fig. 3(b), (d), and (f)), with the highest volume fraction observed at a tool rotational speed of 1000 rpm (Fig. 3(f)). This suggests that more γ phase can be retained owing to the incomplete α' transformation in the alloyed layers as the alloying content increases.

Fig. 4(a)–(c) show concentration distributions in depth for the alloying tool constituent elements obtained from EPMA results presented in Fig. 2. Fig. 4(d)–(f) show the volume fraction of the retained γ distributed in depth obtained from EBSD results presented in Fig. 3. For comparison, depth distributions of Vickers hardness measured at the same positions are shown in Fig. 4(g)–(i). The yellow areas in each graph indicate the range of alloyed layers. The alloyed layers primarily contained W derived from WC particles in the tool. At tool rotational speeds of 600 and 800 rpm, the W contents were less than 5 mass% (Fig. 4(a) and (b)), with a slight increase in the volume fraction of the retained γ observed near the surface (Fig. 4(d) and (e)). Increasing the rotational speed to 1000 rpm resulted in the maximum W content and volume fraction of the retained γ increasing to approximately 8.5 mass% (Fig. 4(c)) and 21 vol% (Fig. 4(f)), respectively, near the surface. As shown in Fig. 4(g)–(i), the hardness of non-alloyed stir zones at any FSP condition was approximately 400 HV, higher than that of the base metal (approximately 160 HV) owing to the formation of α' structure. Furthermore, the maximum hardness measured in the alloyed layers at 600 and 800 rpm was approximately 750 HV near the surface, increasing to approximately 900 HV at 1000 rpm. Thus, the maximum hardness measured in the alloyed layers at 1000 rpm was approximately 500 HV higher than that of non-alloyed stir zones, suggesting a considerable increase owing to solid solution and grain refinement hardening in the α' structure. While the grain size in the alloyed layer was relatively uniform at each rotational speed (Fig. 3), the distributions

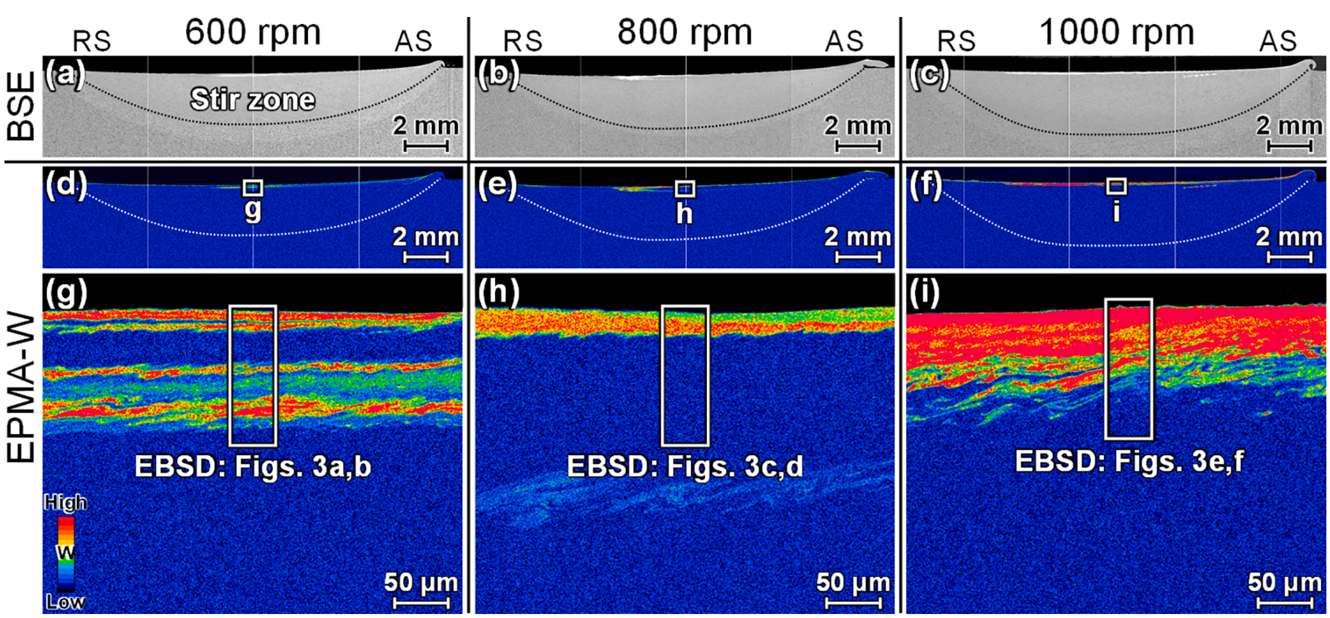

Fig. 2. (a)–(c) BSE images and (d)–(f) EPMA-W maps of the cross-sections of the FSPed steel plates at tool rotational speeds of 600, 800, and 1000 rpm. (g)–(i) The enlarged EPMA-W maps of the white rectangular areas shown in (d)–(f), respectively.

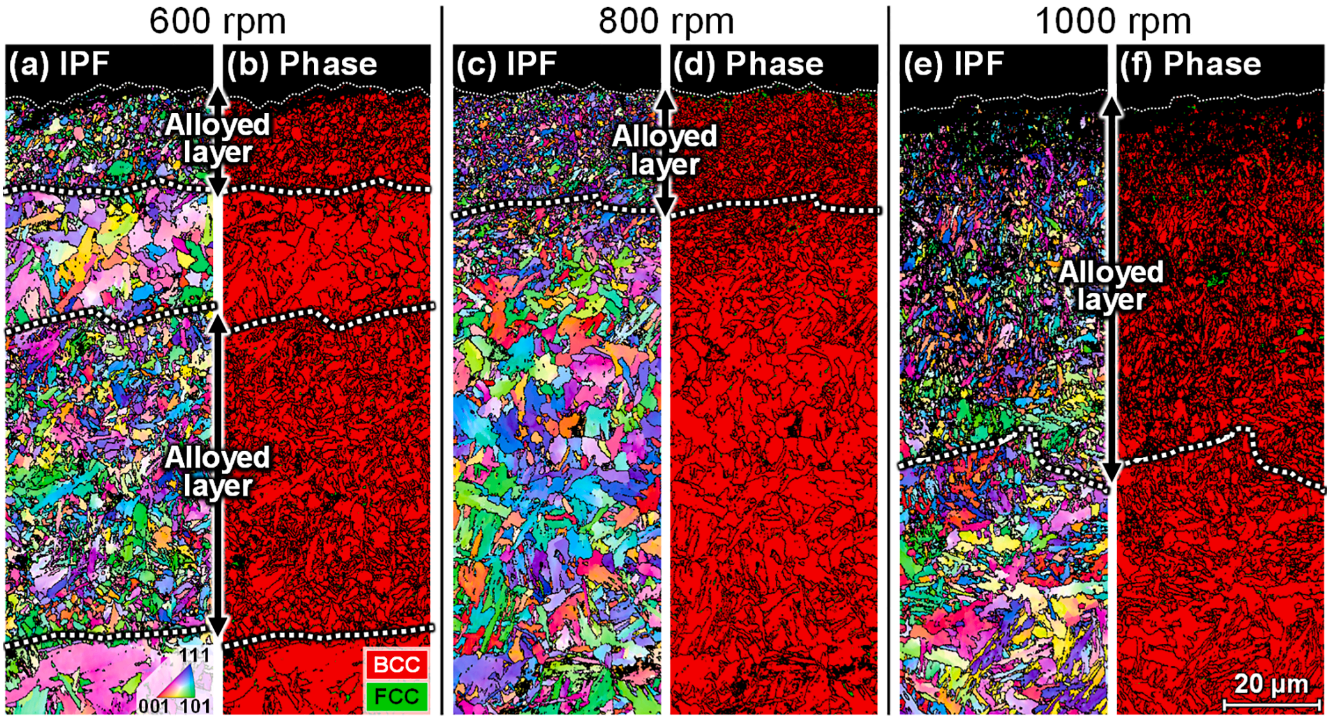

Fig. 3. (a), (c), (e) EBSD-IPF and (b), (d), (f) phase maps obtained from the white rectangular areas in Fig. 2(g)–(i). The alloyed layers are indicated by white broken lines. In the phase maps, red areas represent the BCC (α′) phase, and green areas represent the FCC (γ) phase. (For interpretation of the references to colour in this figure legend, the reader is referred to the web version of this article.)

of alloying contents gradated, corresponding well to the hardness distributions. The supersaturated solid solution of the tool constituent elements in the α′ matrix may contribute more to the hardness increase.

3.2. Residual stress and alloying content in the FSPed steel surface

Residual stresses applied to the stir zone surface were measured via the $\sin^2\psi$ method using the μ-XRD system, and their relationships with alloying contents and microstructure in the stir zone, depending on the tool rotational speed, were investigated. Fig. 5 shows variations of residual stresses in directions parallel and perpendicular to the FSP direction with distance from the FSP center. Uniform compressive residual stresses were observed on both sides of the base metal along parallel and perpendicular directions. However, in the gray area indicating the stir zone, a mixture of tensile and compressive residual stresses was observed, contrary to the typical scenario where only tensile residual stresses are present on the surface of stir zones produced by conventional FSP and FSW [30–33]. The intensity of residual stress changes appeared small at 600 and 800 rpm but increased considerably at 1000. In the stir zone perpendicular to the FSP direction, the residual stress shifted slightly toward the compressive side from 600 to 800 rpm. However, at 1000 rpm, this change considerably increased in the range from −220 to 490 MPa. Similarly, in directions parallel to the FSP direction, the change ranged from −300 to 625 MPa.

In general, the residual stress is determined by the balance between local expansion and contraction of the material, leading to the application of compressive and tensile stresses, respectively. The α′ transformation from the γ phase involves expansion, contrasting with continuous thermal contraction during cooling. The compressive residual stress applied on the surface of stir zones may be caused by α′ transformation expansion near room temperature, which is higher than the tensile stress applied through the thermal contraction. The nonuniform distribution of these stresses in the stir zone, particularly at 1000 rpm, appears to be related to not only the nonuniform distribution of alloying contents but also the formation of the retained γ in the alloyed layer, as shown in Figs. 2–4. Therefore, the α′ start temperature (Ms) is expected to be crucial in applying compressive residual stress and forming the retained γ. The Ms can be estimated based on the alloying contents in steels using Eq. (1) [35] as follows:

$$\mathrm{Ms}\,(^{\circ}C) = 499 - 324\mathrm{C} - 32.4\mathrm{Mn} - 27\mathrm{Cr} - 16.2\mathrm{Ni} - 10.8(\mathrm{Si} + \mathrm{Mo} + \mathrm{W}) \tag{1}$$

where each atomic symbol represents the mass% of the corresponding element. The Ms was obtained at each residual stress measuring point to investigate the mechanism of residual stress application to the stir zone. The FSPed steel plate was cut along the line measuring the residual stress, as shown in Fig. 1, and the alloying contents were measured on the cross section approximately 10–20 μm below each residual stress measuring point using EPMA. The Ms was then estimated based on Eq. (1). Additionally, the volume fraction of the retained γ was measured at each residual stress measuring point using the XRD peaks of α′ and γ phases. Since the penetration depth of X-ray is estimated to be around 15 μm from a steel surface, the relationship between the μ-XRD results and the Ms obtaind using EPMA in each measuring point can be correlated. Fig. 6 illustrates the variation of residual stresses parallel and perpendicular to the FSP direction, along with the volume fraction of the retained γ, with respect to the Ms. The horizontal axis in each graph represents decreasing Ms, indicating an increase in alloying contents. Initially, in the relatively high-Ms region (Fig. 6(a) and (b)), the tensile residual stress in both directions decreased and shifted to compressive residual stress as the Ms decreased. The maximum compressive residual stress in both directions was observed at an Ms of approximately 150 °C. However, further decreasing the Ms below approximately 150 °C in the relatively low-Ms region led to a decrease in compressive residual stress and a shift back to tensile residual stress, consistent with the results obtained at a tool rotational speed of 1000 rpm. This trend is also reflected in the variation of the volume fraction of the retained γ with the Ms, as shown in Fig. 6(c). In the relatively high-Ms region, the volume fraction of the retained γ remained stable at approximately 10 vol%. Conversely, decreasing the Ms below 150 °C correlated closely with an

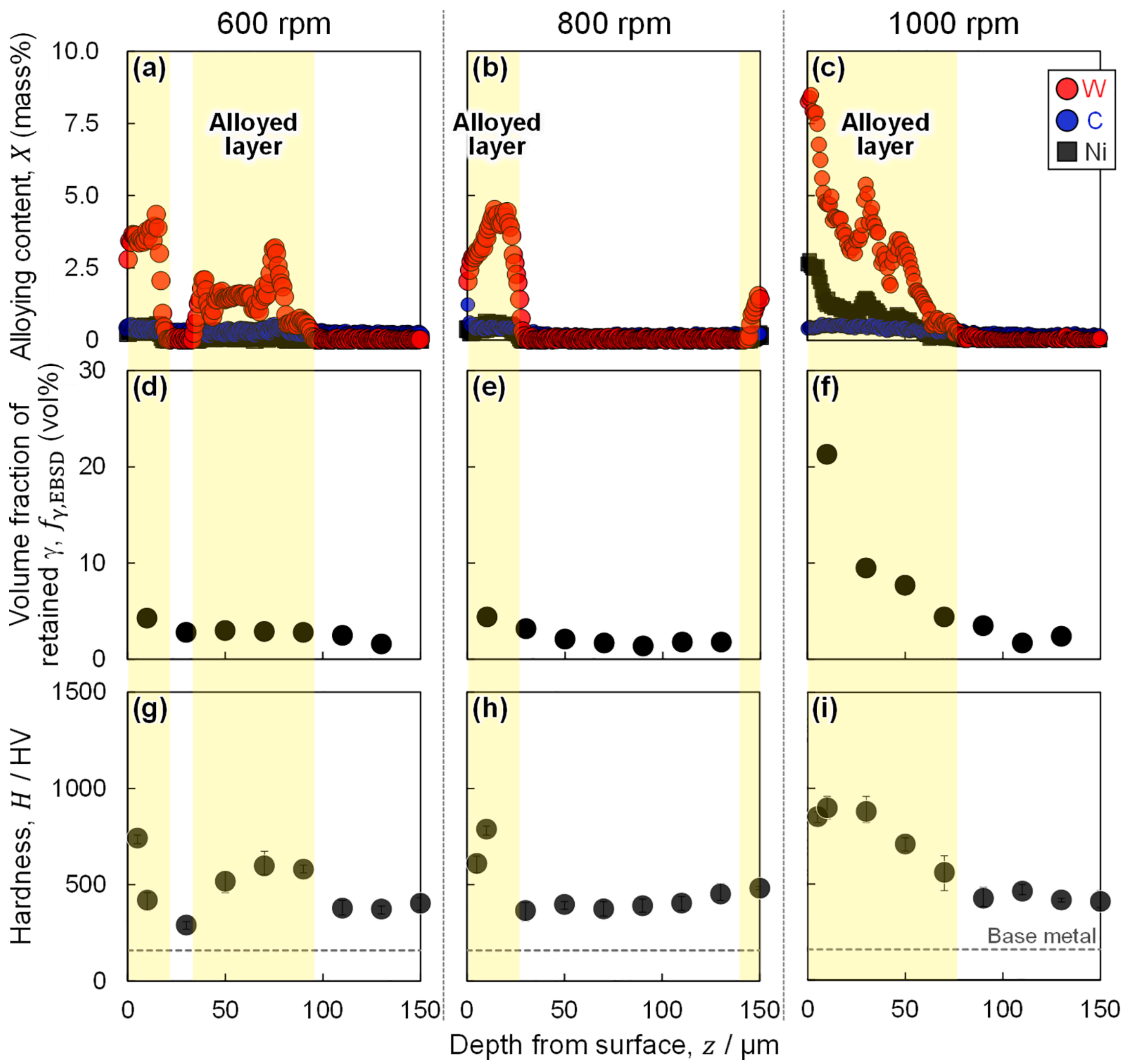

Fig. 4. Depth distributions of (a)–(c) contents of alloying tool constituent elements W, C, and Ni, (d)–(f) the volume fraction of the retained γ, and (g)–(i) Vickers hardness measured at the same positions beneath the stir zone surface at tool rotational speeds of 600, 800, and 1000 rpm. The range of alloyed layers is highlighted in yellow. (For interpretation of the references to colour in this figure legend, the reader is referred to the web version of this article.)

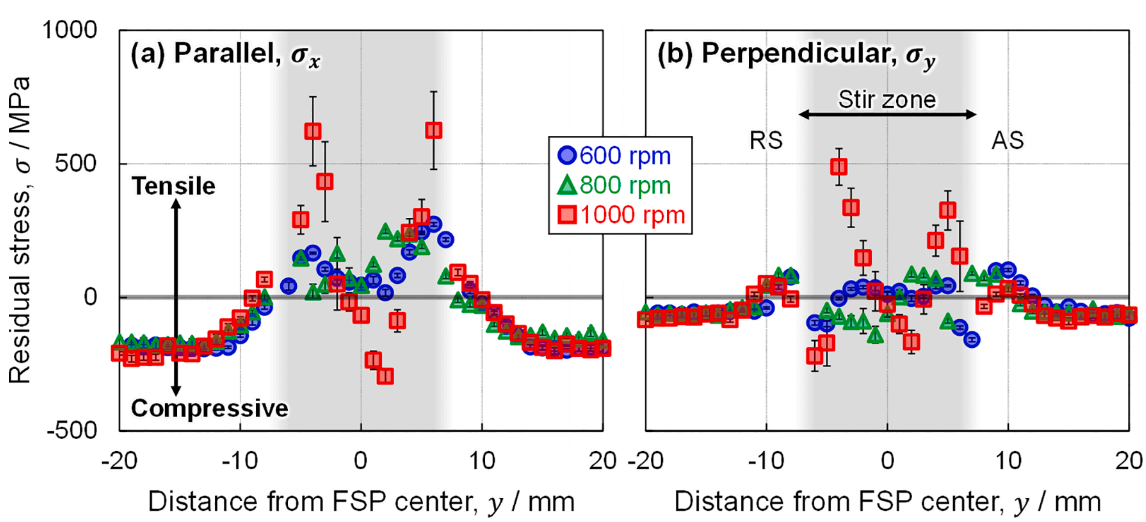

Fig. 5. Variations of residual stresses in the (a) parallel and (b) perpendicular directions to the FSP direction with distance from the FSP center, measured on the FSPed steel plates at tool rotational speeds of 600, 800, and 1000 rpm. The gray area indicates the range of the stir zone.

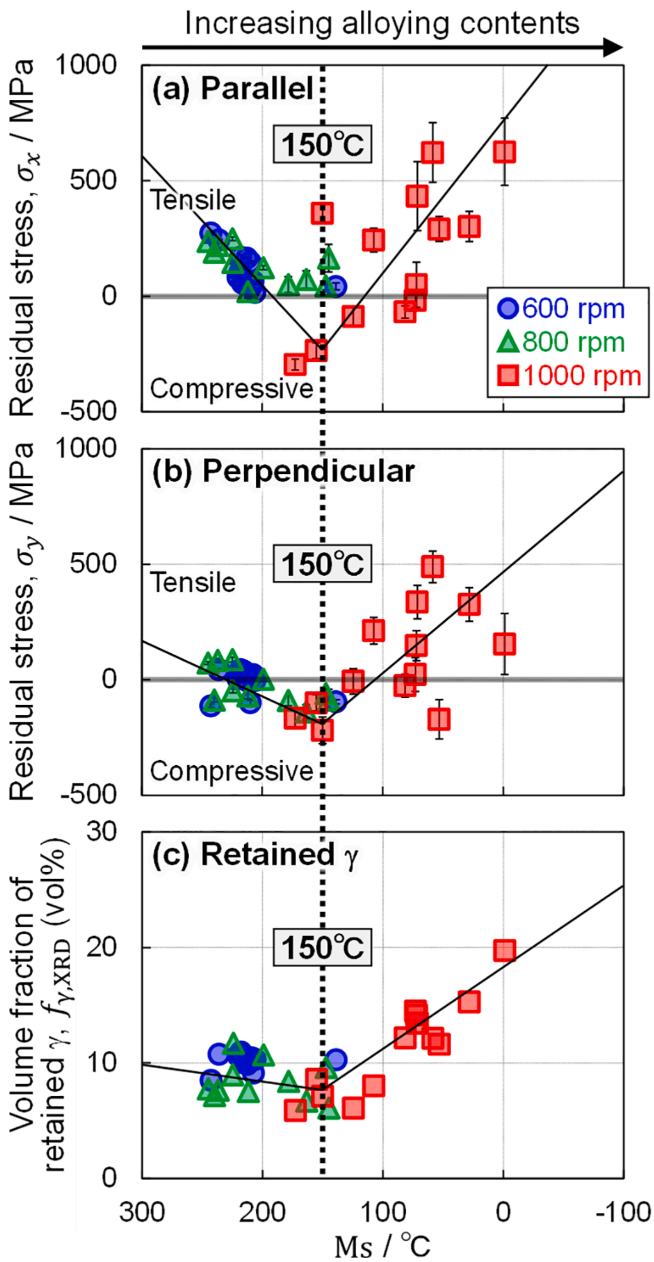

Fig. 6. Dependence of residual stresses on Ms in (a) parallel and (b) perpendicular directions to the FSP direction, and (c) the volume fraction of the retained γ in the stir zone surface FSPed at tool rotational speeds of 600, 800, and 1000 rpm.

increase in the retained γ, accompanied by a decrease in compressive residual stress and a shift to tensile residual stress in the relatively low-Ms region. The volume fraction of retained γ at the Ms around 0 °C (the W and C contents are approximately 8.98 and 0.99 mass%, respectively) was only approximately 20 vol%, attributed to the large deviation from the range of the chemical composition of steels used for Eq. (1) [35]. The actual Ms at 1000 rpm may be expected to be higher. It is noteworthy that the volume fraction of the retained γ measured via XRD tended to be slightly larger than that measured by EBSD (Fig. 4(d)–(f)), likely owing to a detection limit for small retained γ grains in EBSD.

Based on the above-mentioned findings, the mechanism of applying compressive residual stress is discussed, which depends on the alloying content of tool constituent elements and the related Ms. Residual stress distributions showed no fixed pattern with respect to the tool rotational speeds (Fig. 5), although an increase in the tool rotational speed for conventional FSP and FSW may increase both thermal and mechanical strains depending on frictional heat and plastic deformation, respectively, resulting in a monotonous increase in the tensile residual stress. However, in their variation with Ms (Fig. 6(a) and (b)), the Ms range was effectively divided by the tool rotational speed, and a proportional relationship to Ms was observed. This suggests that the alloying contents is dominant for the residual stress change rather than the thermal and mechanical strains caused by the tool motion. In other words, the residual stress applied to the topmost layer of FSPed steel plates can be controlled by the alloying contents depending on the tool rotational speed. At tool rotational speeds of 600 and 800 rpm, the stir zones were partially covered with lower alloying contents, resulting in tensile residual stress. This suggests that the α′ transformation was completed at a higher temperature, and its volume expansion was negated by thermal contraction during an extended cooling period. The transition from tensile to compressive residual stress, with compression maximized at approximately 150 °C, can be attributed to α′ transformation expansion near room temperature. Conversely, at 1000 rpm, the residual stress increased excessively with decreasing Ms owing to increased alloying contents. This indicates that the α′ transformation could not be completed near room temperature, resulting in less α′ transformation expansion, along with an increase in the volume fraction of the retained γ. This scenario resembles the use of low transformation temperature (LTT) welding materials developed to enhance the fatigue strength of welded steel joints through α′ transformation expansion [36,37]. In LTT welding materials, the Ms is primarily lowered by Ni and Cr contents (W and C contents in this study), as referenced in Eq. (1). Experimental evidence suggests that the α′ transformation expansion strain at room temperature reaches a maximum of approximately 0.6 % when Ms is approximately 150 °C, leading to compressive residual stress applied to the weld toe surface. In FSP accompanied by alloying with W and C elements, rotational speeds between 800 and 1000 rpm are crucial for achieving an Ms of approximately 150 °C and applying compressive residual stress. The advantage of this FSP technique lies in the formation of ultrafine-grained structures in a solid state, compared to LTT welding materials, which are associated with risks of solidification cracking and toughness degradation owing to grain coarsening in the weld metals.

3.3. Effect of retained γ on mechanical properties of the FSPed steel surface

Further decreasing Ms with increasing alloying contents of tool constituent elements such as W and C in the topmost layer of the FSPed steel plate at a rotational speed of 1000 rpm resulted in the application of tensile residual stress and the formation of the retained γ. Typically, tensile residual stress deteriorates fatigue strength by accelerating crack propagation. However, the topmost layer in the FSPed steel plate contained the retained γ, which is expected to suppress crack propagation owing to deformation-induced α′ transformation at the crack tip during fatigue [38,39]. To investigate the stability of the retained γ in the alloyed topmost layer responding to plastic deformation, a tensile test was conducted using small, thin specimens with a thickness of approximately 0.1 mm (testable limit). The stir zone specimens with and without the alloyed topmost layer, approximately 100 μm thick, at the tool rotational speed of 1000 rpm were taken from depths of approximately 0–0.1 and 0.1–0.2 mm from the surface, respectively. For comparison, a thermally α′-transformed specimen was prepared using sub-zero treatment to reduce the volume fraction of the retained γ. The stress–strain curves of these stir zone specimens, along with that of the base metal specimen, are shown in Fig. 7. The average volume fraction of the retained γ measured on the parallel section surface of each specimen before testing is indicated near the corresponding curve. The specimen with the alloyed topmost layer had an average volume fraction of the retained γ estimated to be approximately 20.6 vol%, reduced to 16.1 vol% by the sub-zero treatment. In contrast, those in the specimens without the alloyed topmost layer and taken from the base metal were 0

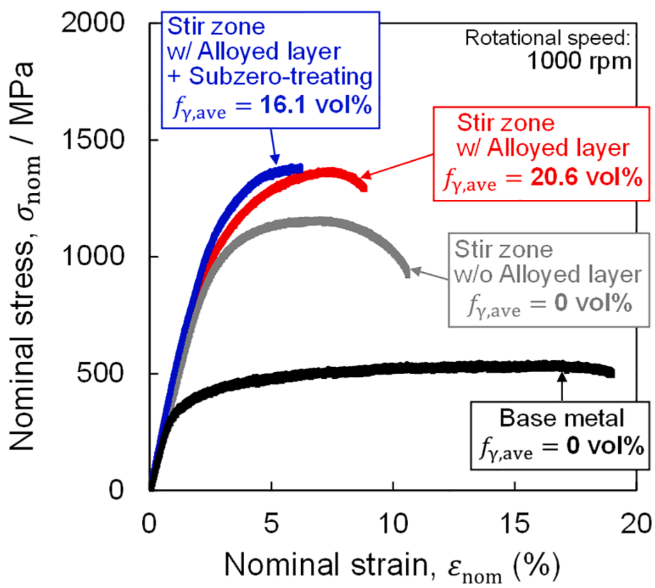

Fig. 7. Stress–strain curves from tensile specimens extracted from the stir zone with and without the alloyed topmost layer at a tool rotational speed of 1000 rpm. Two types of specimens with the alloyed topmost layer, one with and one without sub-zero treatment, are presented alongside that of the base metal for comparison. The $f_{\gamma,ave}$ denotes the average volume fraction of the retained γ measured on the parallel section surface of each specimen before testing.

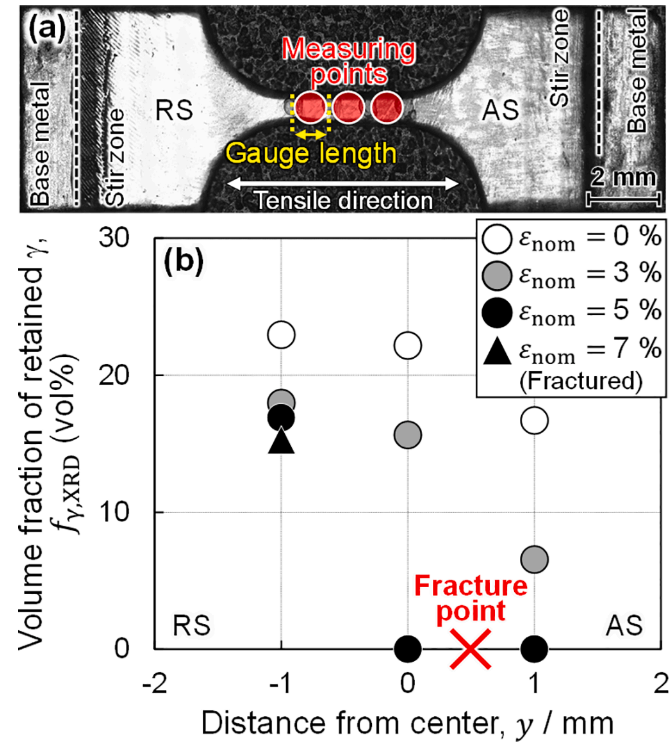

Fig. 8. (a) Optical image of a tensile specimen extracted from the stir zone with the alloyed topmost layer. (b) The volume fraction of the retained γ measured at three red circles (−1, 0, and 1 mm away from the center position of a specimen parallel section in (a)) at nominal strains of 0 %, 3 %, 5 %, and 7 %. (For interpretation of the references to colour in this figure legend, the reader is referred to the web version of this article.)

vol%. The tensile strength of the base metal specimen was approximately 550 MPa, close to the standard tensile strength of SM490A low-carbon steel plate, indicating the suitability of the small specimens used in this study without the sizing effect. Remarkably, in all the other three specimens, the tensile strength increased more than twice that of the base metal specimen, with the elongation reduced to half or less than that of the base metal specimen. The specimens with the alloyed topmost layer exhibited a tensile strength of approximately 1380 MPa, regardless of the sub-zero treatment, which was approximately 230 MPa higher than that in the specimen without the alloyed topmost layer. The increment of tensile strength owing to the alloyed topmost layer can be attributed to solid solution and grain refinement hardening in the α′ structure resulting from alloying the tool constituent elements. Additionally, in the specimen without the sub-zero treatment, further plastic deformation may occur owing to the increased retained γ, leading to larger elongation compared to the specimen with the sub-zero treatment. While there is a trade-off relationship between strength and ductility in metallic materials, the elongation improved without lowering the tensile strength can be a specific benefit of the deformation-induced α′ transformation.

To track the deformation-induced α′ transformation of the retained γ during the tensile test, the volume fraction of the retained γ on the parallel section surface of a tensile specimen with the alloyed topmost layer (red curve in Fig. 7) was measured using the μ-XRD system − 1, 0, and 1 mm away (indicated by three red circles in Fig. 8(a)) from the center position of a specimen parallel section, as depicted in an optical image of the specimen (Fig. 8(a)). Fig. 8(b) shows the volume fraction of the retained γ measured at each nominal strain of 0 %, 3 %, 5 %, and 7 % at the three red circles. The initial volume fraction of the retained γ before testing was estimated to be approximately 23, 22, and 17 vol% at the measuring points of − 1, 0, and 1 mm away from the center position of the specimen parallel section, respectively. The nonuniform distribution of retained γ can correspond to the nonuniform distribution of alloying contents on the specimen surface. Across all three measuring points, the volume fraction of the retained γ decreased with increasing nominal strain. At the measuring points of $y = 0$ and 1 mm, it decreased to 0 vol% at the nominal strain of 5 %, and further increasing the nominal strain up to 7 % resulted in specimen failure between the two measuring points. At the same nominal strain of 7 %, the volume fraction of retained γ at the measuring point of $y = -1$ mm was estimated to be approximately 15 %. At each nominal strain, the local strain at the three measuring points was estimated based on the displacement between black lines to the right and left of each measuring circle, and its relationship with the decrease in volume fraction of the retained γ is shown in Fig. 9. The volume fraction of the retained γ decreased exponentially with increasing local strain, indicating deformation-induced α′ transformation of the retained γ. This highlights the significant role of the volume fraction of retained γ in the ductility of the specimen part. Generally, plastic deformation can continue in the retained γ in the specimen, leaving behind the transformed α′. In the present tensile test, local plastic deformation seemed to be concentrated at the measuring points of $y = 0$ and 1 mm at a nominal strain of 5 %, ultimately leading to fracture. At the beginning of the tensile test, deformation-induced α′ transformation occurred homogeneously in the specimen. With plastic deformation, stress and strain concentration occurred in the necking part where a small number of the retained γ was left. Even with the hardened α′ at the necking part, minimizing the cross-sectional area can prove fatal in this small specimen.

To further explore the influence of the retained γ on fatigue crack propagation, fatigue crack propagation tests were conducted. CT specimens were extracted, with and without the alloyed topmost layer, from the depth ranges of approximately 0–1.3 and 0.2–1.5 mm (with a specimen thickness of 1.3 mm), respectively, from the surface of the stir zone produced at a rotational speed of 1000 rpm. The residual stresses applied to these CT specimen surfaces fluctuated within ± 50 MPa owing to cutting and thinning during specimen preparation. The results are summarized in Fig. 10. Across all stress intensity factor ranges, the crack propagation rate of specimens with the alloyed topmost layer was consistently lower compared to those without it (Fig. 10(a)). The

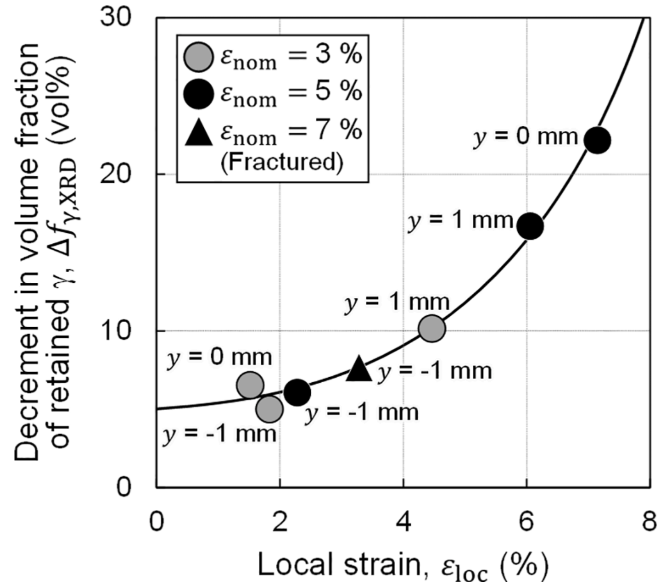

Fig. 9. Relationship between local strain estimated from the displacement between black lines to the right and left of each measuring point in the tensile specimen in Fig. 8(a) and decrement in the volume fraction of the retained γ at each measuring point, estimated based on Fig. 8(b).

reduction in crack propagation rate attributed to the alloyed topmost layer exceeded 40 %, and this effect increased up to 60 % with higher stress intensity factor ranges (Fig. 10(b)). These results indicate that the alloyed topmost layer effectively mitigated crack propagation, with the extent of suppression increasing with higher stress intensity factor ranges.

Fig. 11(a) shows an optical image capturing the top surface of the CT specimen featuring the alloyed topmost layer after the fatigue crack propagation test. Enlarging the V-notch tip portion, Fig. 11(b) reveals a linearly propagated crack ahead of the notch tip. For closer inspection, the fracture surface underwent SEM analysis at positions every 2 mm from the V-notch tip. As illustrated in Fig. 11(c), SEM images show the fracture surface evolution along the crack propagation path, highlighting the alloyed topmost layer in the upper segment. The thickness of this layer, approximately 100 μm, is shown in Fig. 2(i). The enlarged fracture surfaces taken from the positions with alphabetic characters in Fig. 11(c) are shown in Fig. 11(d)–(k). Notably, clear striations are discernible in regions without the alloyed topmost layer at the lower portion of the CT specimen (Fig. 11(h)–(k)). Conversely, the fracture surface in the alloyed topmost layer on the upper part exhibits a less defined surface morphology owing to the finer spacing of striations (Fig. 11(d)–(g)). The striation spacing indicates the fatigue crack propagation distance per cycle under cyclic loads, suggesting that the crack propagation rate decreased as the alloyed topmost layer was approached.

To understand why the alloyed topmost layer decreased crack propagation rates as stress intensity factor ranges increased, microstructural examinations were conducted near the crack using EBSD. The cross-sectional OM images and EBSD-IPF and phase maps in Fig. 12 illustrate observations taken approximately 2, 4, 6, and 8 mm from the V-notch tip of the CT specimen featuring the alloyed topmost layer. The uniformly distributed alloyed topmost layers, approximately 100 μm thick, are visible in bright contrast on the upper part (depicted in Fig. 12(a)–(d)). EBSD observation zones were positioned adjacent to the crack on the upper and lower parts of the CT specimen (outlined by white rectangles in Fig. 12(a)–(d)). The EBSD-IPF maps from the upper sections reveal that the alloyed topmost layer comprises notably finer grains compared to the lower sections lacking this layer (presented in Fig. 12(e-1)–(l-1)). Additionally, the retained γ is predominantly found

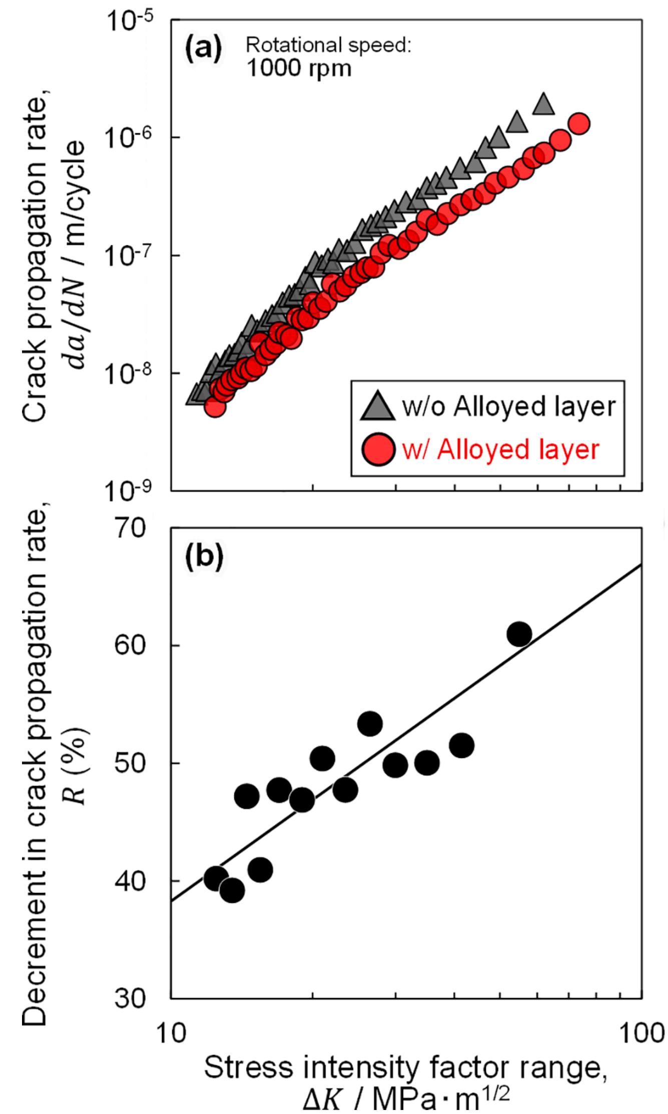

Fig. 10. (a) Fatigue crack propagation rates of the CT specimens with and without the alloyed topmost layer. (b) The decrease in fatigue crack propagation rate attributed to the presence of the alloyed topmost layer owing to variation in the stress intensity factor range. These specimens were extracted from the stir zone surface generated at a tool rotational speed of 1000 rpm.

in the alloyed topmost layers, highlighted in green in the EBSD-phase maps, with its volume fraction appearing to decrease as the distance from the V-notch tip increases (as depicted in Fig. 12(e-2)–(h-2)). Conversely, almost no retained γ is observed at any position in the lower sections lacking the alloyed topmost layer (illustrated in Fig. 12(i-2)–(l-2)).

Fig. 13 shows the volume fraction of the retained γ, estimated from the EBSD-phase maps depicted in Fig. 12(e-2)–(l-2), as it varies with distance from the V-notch tip and the corresponding stress intensity factor range. On the lower part lacking the alloyed topmost layer, the volume fraction of the retained γ remained approximately 2 vol% across all distances from the V-notch tip, consistent with pretesting levels. Conversely, on the upper part featuring the alloyed topmost layer, the volume fraction of the retained γ decreased from approximately 15 vol% (consistent with pretesting levels) with increasing distance from the V-notch tip and stress intensity factor range. It reached approximately 5 vol% at approximately 8 mm from the V-notch tip. This reduction suggests that the retained γ in the alloyed topmost layer suppressed crack propagation by undergoing deformation-induced α′ transformation. The

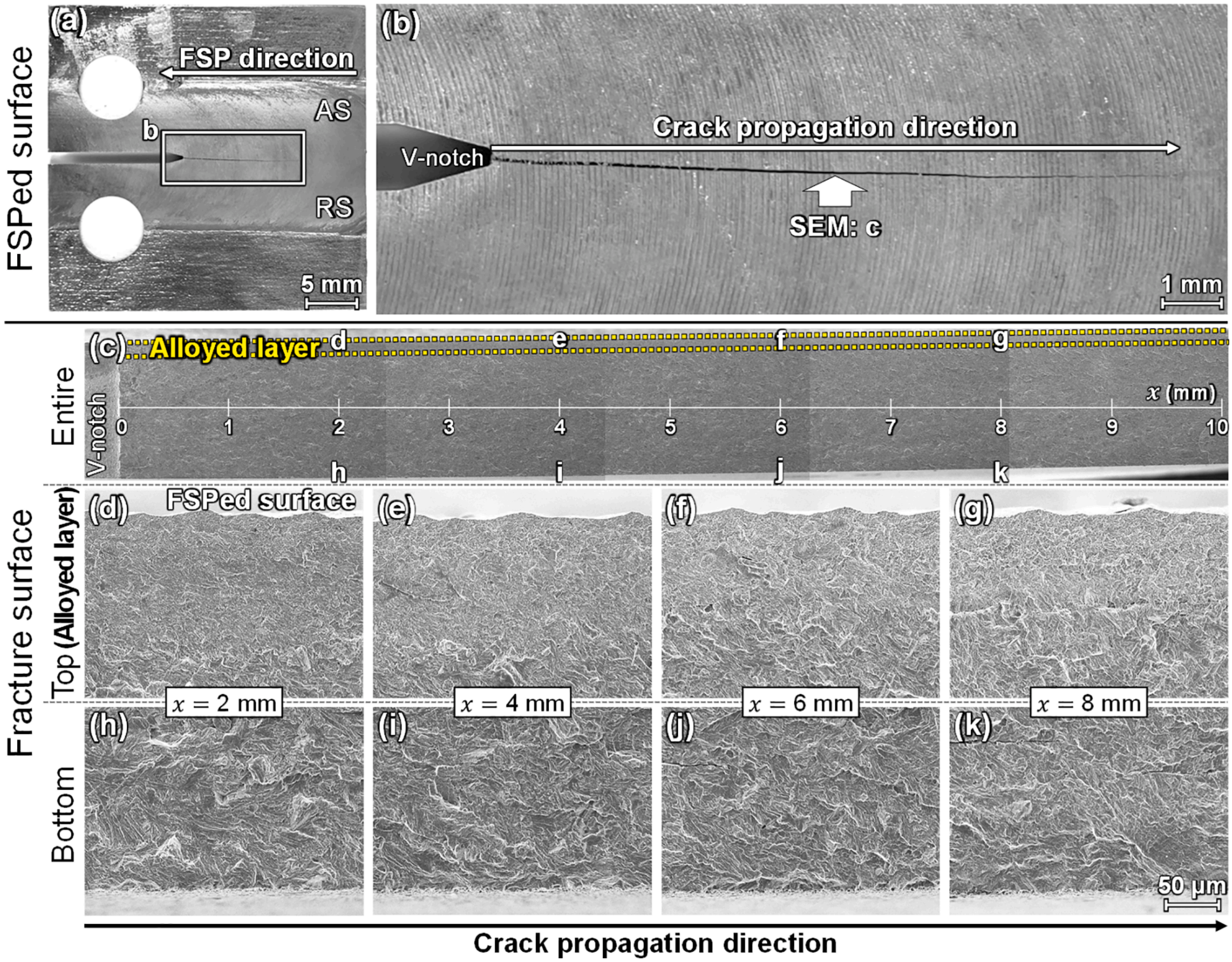

Fig. 11. (a) Optical image of the top surface of the CT specimen taken from the stir zone with the alloyed topmost layer after the fatigue crack propagation test and (b) the enlarged view around the crack propagated from the V-notch tip. (c) An SEM image of the fatigue fracture surface, and (d)–(g) the enlarged view at positions with alphabetic characters of d–k in c at distances of approximately 2, 4, 6, and 8 mm from the V-notch tip.

volume expansion resulting from this transformation likely contributed to crack closure, similar to compressive residual stress, thus impeding crack propagation. The decline in crack propagation rate during later stages may be attributed to increased α' transformation expansion corresponding to the rising stress intensity factor range. Therefore, increasing the retained γ through excessive reduction of Ms below approximately 150 °C, alongside increased alloying contents, could curb lateral crack propagation along the surface despite concurrent increment in tensile residual stress with the increasing retained γ. In our previous studies [10,11], fatigue cracks tended to initiate at weld toe surfaces that corresponded to the end of or a little apart from the alloyed topmost layer with a significant hardness increase. The surface modification, forming the alloyed topmost layer, would also aid in suppressing crack initiation.

4. Conclusions

FSP was performed on a low-carbon steel plate using a WC tool at various rotational speeds to elucidate the mechanism of compressive residual stress application to the stir zone surface. This study evaluated the influence of alloying contents of the tool constituent elements on the microstructure and mechanical properties of the resulting FSPed surfaces. The important findings of this study are as follows:

1) The surface of FSPed steel underwent alloying with tool constituent elements such as W, C, and Ni, with total alloying contents showing an upward trend with increasing tool rotational speed. The resultant alloyed topmost layer exhibited a lath α' structure with a small amount of the retained γ depending on the alloying contents. The hardness increase with increasing tool rotational speed is attributed to solid solution and grain refinement hardening.
2) Residual stresses exhibited nonuniform variations with the distance from the FSP center but uniformly responded to changes in alloying contents and the related Ms. In the relatively high-Ms region, tensile residual stress decreased and changed to compressive residual stress with increasing alloying contents and reduced Ms. Subsequent decrease of Ms below 150 °C resulted in decreased compressive residual stress, reverting to tensile residual stress. The compressive residual stresses, which peaked at an Ms of approximately 150 °C, can be attributed to the completion of the α' transformation near room temperature. The presence of the retained γ indicates incomplete α' transformation at room temperature, resulting in insufficient volume expansion to apply compressive residual stress.
3) Tensile tests showed that specimens featuring the alloyed topmost layer exhibited the highest tensile strength, reaching approximately 1380 MPa, surpassing their counterparts lacking this layer by approximately 230 MPa. The decrease in the volume fraction of the retained γ with increasing local strain during testing suggests a

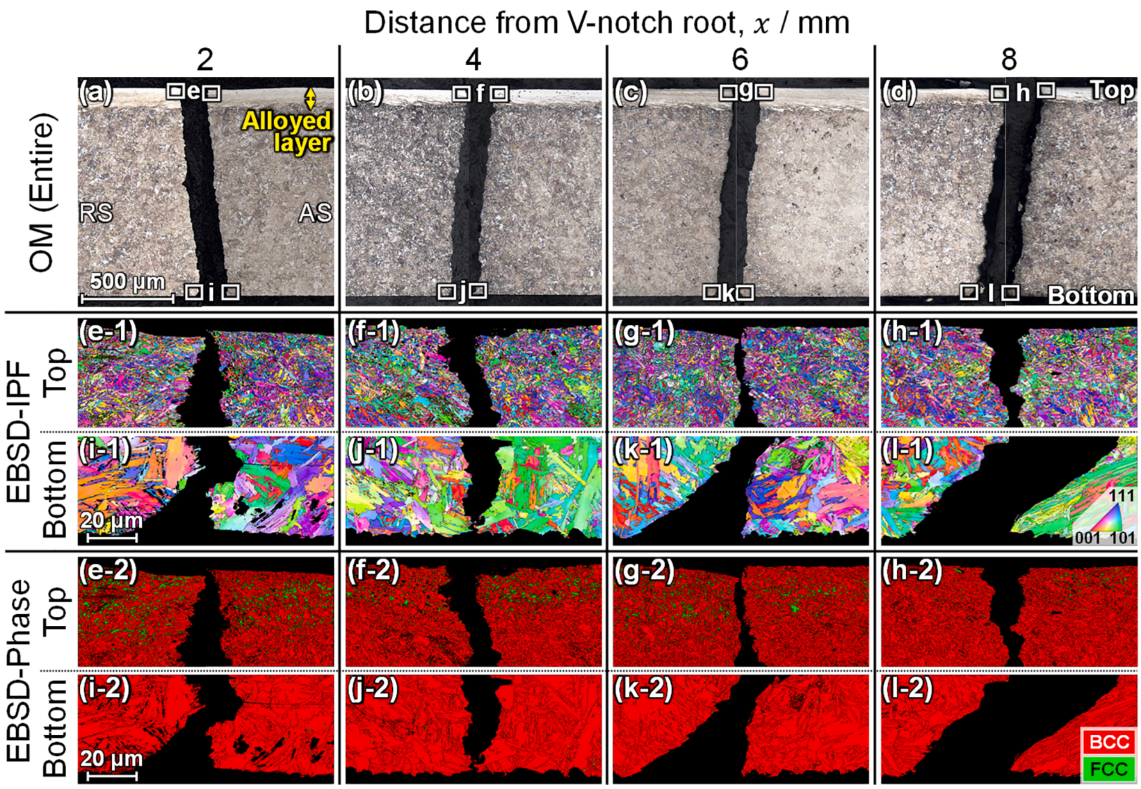

Fig. 12. OM images of the CT specimen with the alloyed topmost layer, captured at various distances from the V-notch tip on the fracture surface of approximately (a) 2, (b) 4, (c) 6, and (d) 8 mm. (e-1)–(l-1) The EBSD-IPF and phase maps obtained within the white rectangles in (a)–(d). In the phase maps, areas colored in red and green represent BCC (α′) and FCC (γ) phases, respectively. (For interpretation of the references to colour in this figure legend, the reader is referred to the web version of this article.)

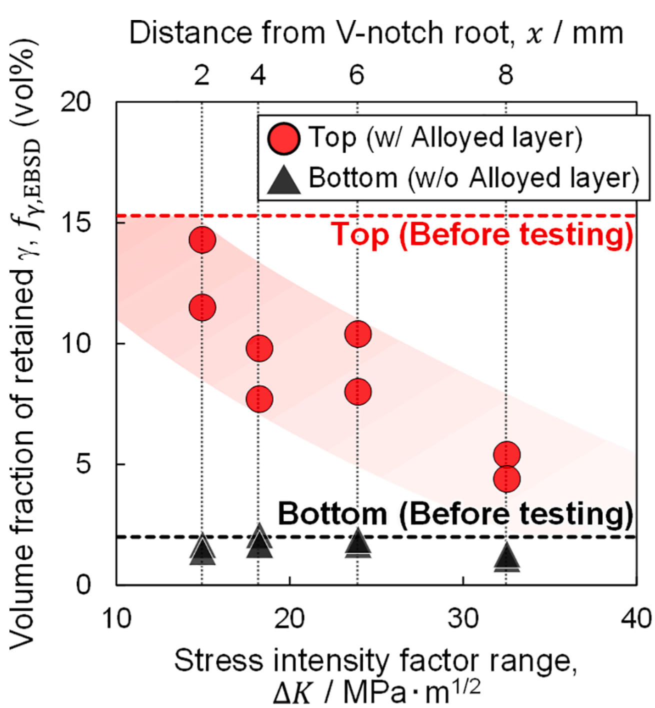

Fig. 13. Volume fraction of the retained γ, estimated from the EBSD-phase maps depicted in Fig. 12(e-2)–(l-2), varying with distance from the V-notch tip in the CT specimen with the alloyed topmost layer and the related stress intensity factor range estimated in the fatigue crack propagation test.

contribution to strain relaxation owing to deformation-induced α′ transformation, thereby enhancing ductility. Fatigue crack propagation showed that the crack propagation rate of specimens with the alloyed topmost layer was 40 %–60 % lower than those without this layer. The deformation-induced α′ transformation during testing suppressed lateral crack propagation, further decreasing the crack propagation rate owing to larger transformation expansion corresponding to increased stress intensity factor range.

CRediT authorship contribution statement

Hajime Yamamoto: Writing – original draft, Visualization, Validation, Methodology, Investigation, Funding acquisition, Formal analysis, Data curation, Conceptualization. **Yuji Yamamoto:** Methodology, Investigation, Formal analysis, Data curation. **Kazuhiro Ito:** Writing – review & editing, Supervision, Project administration, Conceptualization. **Yoshiki Mikami:** Methodology, Data curation.

Declaration of competing interest

The authors declare the following financial interests/personal relationships which may be considered as potential competing interests: [Hajime Yamamoto reports financial support was provided by Japan Society for the Promotion of Science. Hajime Yamamoto reports financial support was provided by Amada Foundation. If there are other authors, they declare that they have no known competing financial interests or personal relationships that could have appeared to influence the work reported in this paper.].

Data availability

Data will be made available on request.

Acknowledgements

This work was supported by JSPS KAKENHI Grant Number 21K14438 and the Amada Foundation Grant Number AF-2020032-C2.

References

[1] J. Lago, L. Trško, M. Jambor, F. Nový, O. Bokůvka, M. Mičian, F. Pastorek, Fatigue life improvement of the high strength steel welded joints by ultrasonic impact peening, Metals 9 (2019) 619, https://doi.org/10.3390/met9060619.
[2] R. Fueki, K. Takahashi, Improving the fatigue limit and rendering a defect harmless by laser peening for a high strength steel welded joint, Opt. Laser Technol. 134 (2021) 106605, https://doi.org/10.1016/j.optlastec.2020.106605.
[3] M.P. Aung, H. Katsuda, M. Hirohata, Fatigue-performance improvement of patch-plate welding via PWHT with induction heating, J. Constr. Steel Res. 160 (2019) 280–288, https://doi.org/10.1016/j.jcsr.2019.05.047.
[4] X. Feng, K. Zheng, J. Heng, J. Zhu, X. He, Fatigue performance of rib-to-deck joints in orthotropic steel deck with PWHT, J. Constr. Steel Res. 196 (2022) 107420, https://doi.org/10.1016/j.jcsr.2022.107420.
[5] Z. Fu, B. Ji, X. Kong, X. Chen, Grinding treatment effect on rib-to-roof weld fatigue performance of steel bridge decks, J. Constr. Steel Res. 129 (2017) 163–170, https://doi.org/10.1016/j.jcsr.2016.09.018.
[6] I.T. Kim, H.S. Kim, D.K. Dao, J.H. Ahn, Y.S. Jeong, Fatigue resistance improvement of welded joints by bristle roll-brush grinding, Int. J. Steel Struct. 18 (2018) 1631–1638, https://doi.org/10.1007/s13296-018-0059-1.
[7] T. Dahle, Design fatigue strength of TIG-dressed welded joints in high-strength steels subjected to spectrum loading, Int. J. Fatigue 20 (1998) 677–681, https://doi.org/10.1016/S0142-1123(98)00031-0.
[8] T. Skriko, M. Ghafouri, T. Björk, Fatigue strength of TIG-dressed ultra-high-strength steel fillet weld joints at high stress ratio, Int. J. Fatigue 94 (2017) 110–120, https://doi.org/10.1016/j.ijfatigue.2016.09.018.
[9] K. Ito, T. Okuda, R. Ueji, H. Fujii, C. Shiga, Increase of bending fatigue resistance for tungsten inert gas welded SS400 steel plates using friction stir processing, Mater. Des. 61 (2014) 275–280, https://doi.org/10.1016/j.matdes.2014.04.076.
[10] H. Yamamoto, Y. Danno, K. Ito, Y. Mikami, H. Fujii, Weld toe modification using spherical-tip WC tool FSP in fatigue strength improvement of high-strength low-alloy steel joints, Mater. Des. 160 (2018) 1019–1028, https://doi.org/10.1016/j.matdes.2018.10.036.
[11] H. Yamamoto, S. Koga, K. Ito, Y. Mikami, Fatigue strength improvement due to alloying steel weld toes with WC tool constituent elements through friction stir processing, Int. J. Adv. Manuf. Technol. 119 (2022) 6203–6213, https://doi.org/10.1007/s00170-022-08690-7.
[12] R.S. Mishra, Z.Y. Ma, Friction stir welding and processing, Mater. Sci. Eng. R 50 (2005) 1–78, https://doi.org/10.1016/j.mser.2005.07.001.
[13] D. Yadav, R. Bauri, Effect of friction stir processing on microstructure and mechanical properties of aluminium, Mater. Sci. Eng. A 539 (2012) 85–92, https://doi.org/10.1016/j.msea.2012.01.055.
[14] J. Su, J. Wang, R.S. Mishra, R. Xu, J.A. Baumann, Microstructure and mechanical properties of a friction stir processed Ti–6Al–4V alloy, Mater. Sci. Eng. A 573 (2013) 67–74, https://doi.org/10.1016/j.msea.2013.02.025.
[15] D.M. Sekban, S.M. Aktarer, P. Xue, Z.Y. Ma, G. Purcek, Impact toughness of friction stir processed low carbon steel used in shipbuilding, Mater. Sci. Eng. A 672 (2016) 40–48, https://doi.org/10.1016/j.msea.2016.06.063.
[16] P. Xue, B.B. Wang, F.F. Chen, W.G. Wang, B.L. Xiao, Z.Y. Ma, Microstructure and mechanical properties of friction stir processed Cu with an ideal ultrafine-grained structure, Mater. Charact. 121 (2016) 187–194, https://doi.org/10.1016/j.matchar.2016.10.009.
[17] X.C. Luo, L.M. Kang, H.L. Liu, Z.J. Li, Y.F. Liu, D.T. Zhang, D.L. Chen, Enhancing mechanical properties of AZ61 magnesium alloy via friction stir processing: Effect of processing parameters, Mater. Sci. Eng. A 797 (2020) 139945, https://doi.org/10.1016/j.msea.2020.139945.
[18] D.R. Ni, D. Wang, A.H. Feng, G. Yao, Z.Y. Ma, Enhancing the high-cycle fatigue strength of Mg–9Al–1Zn casting by friction stir processing, Scr. Mater. 61 (2009) 568–571, https://doi.org/10.1016/j.scriptamat.2009.05.023.
[19] S. Jana, R.S. Mishra, J.B. Baumann, G. Grant, Effect of friction stir processing on fatigue behavior of an investment cast Al–7Si–0.6 Mg alloy, Acta Mater. 58 (2010) 989–1003, https://doi.org/10.1016/j.actamat.2009.10.015.
[20] R. Kapoor, K. Kandasamy, R.S. Mishra, J.A. Baumann, G. Grant, Effect of friction stir processing on the tensile and fatigue behavior of a cast A206 alloy, Mater. Sci. Eng. A 561 (2013) 159–166, https://doi.org/10.1016/j.msea.2012.10.090.
[21] J.G.S. Macías, C. Elangeswaran, L. Zhao, B.V. Hooreweder, J. Adrien, E. Maire, J. Y. Buffière, W. Ludwig, P.J. Jacques, A. Simar, Ductilisation and fatigue life enhancement of selective laser melted AlSi10Mg by friction stir processing, Scr. Mater. 170 (2019) 124–128, https://doi.org/10.1016/j.scriptamat.2019.05.044.
[22] C. He, J. Wei, Y. Li, Z. Zhang, N. Tian, G. Qin, L. Zuo, Improvement of microstructure and fatigue performance of wire-arc additive manufactured 4043 aluminum alloy assisted by interlayer friction stir processing, J. Mater. Sci. Technol. 133 (2023) 183–194, https://doi.org/10.1016/j.jmst.2022.07.001.
[23] J. Wei, C. He, Y. Zhao, M. Qie, G. Qin, L. Zuo, Evolution of microstructure and properties in 2219 aluminum alloy produced by wire arc additive manufacturing assisted by interlayer friction stir processing, Mater. Sci. Eng. A 868 (2023) 144794, https://doi.org/10.1016/j.msea.2023.144794.
[24] X. Guo, D. Ni, H. Li, P. Xue, R. Xu, Z. Pan, S. Zhou, Z. Ma, Enhancing strength, ductility, and fatigue performance of Al–Zn–Mg–Cu–Sc–Zr alloy using a hybrid approach: Wire-arc directed energy deposition and interlayer friction stir processing, J. Mater. Process. Technol. 322 (2023) 118173, https://doi.org/10.1016/j.jmatprotec.2023.118173.
[25] J. da Silva, J.M. Costa, A.J.M. Loureiro, Ferreira: Fatigue behaviour of AA6082-T6 MIG welded butt joints improved by friction stir processing, Mater. Des. 51 (2013) 315–322, https://doi.org/10.1016/j.matdes.2013.04.026.
[26] L.P. Borrego, J.D. Costa, J.S. Jesus, A.R. Loureiro, J.M. Ferreira, Fatigue life improvement by friction stir processing of 5083 aluminium alloy MIG butt welds, Theor. Appl. Fract. Mech. 70 (2014) 68–74, https://doi.org/10.1016/j.tafmec.2014.02.002.
[27] J.D.M. Costa, J.S. Jesus, A. Loureiro, J.A.M. Ferreira, L.P. Borrego, Fatigue life improvement of mig welded aluminium T-joints by friction stir processing, Int. J. Fatigue 61 (2014) 244–254, https://doi.org/10.1016/j.ijfatigue.2013.11.004.
[28] J.S. Jesus, J.M. Costa, A. Loureiro, J.M. Ferreira, Fatigue strength improvement of GMAW T-welds in AA5083 by friction-stir processing, Int. J. Fatigue 61 (2017) 124–134, https://doi.org/10.1016/j.ijfatigue.2016.12.034.
[29] H. Yamamoto, Y. Imagawa, K. Ito, K. Chen, L. Zhang, Alloying a topmost steel-plate layer with WC-tool constituent elements during friction stir processing, J. Manuf. Process. 69 (2021) 311–319, https://doi.org/10.1016/j.jmapro.2021.07.050.
[30] A. Steuwer, S.J. Barnes, J. Altenkirch, R. Johnson, P.j. Withers, Friction stir welding of HSLA-65 steel: Part II. The influence of weld speed and tool material on the residual stress distribution and tool wear, Metall. Mater. Trans. A 43 (2012) 2356–2365, https://doi.org/10.1007/s11661-011-0643-x.
[31] L.N. Brewer, M.S. Bennett, B.W. Baker, E.A. Payzant, L.M. Sochalski-Kolbus, Characterization of residual stress as a function of friction stir welding parameters in oxide dispersion strengthened (ODS) steel MA956, Mater. Sci. Eng. A 647 (2015) 313–321, https://doi.org/10.1016/j.msea.2015.09.020.
[32] J.W. Sowards, T. Gnäupel-Herold, J.D. McColskey, V.F. Pereira, A.J. Ramirez, Characterization of mechanical properties, fatigue-crack propagation, and residual stresses in a microalloyed pipeline-steel friction-stir weld, Mater. Des. 88 (2015) 632–642, https://doi.org/10.1016/j.matdes.2015.09.049.
[33] H. Dawson, M. Serrano, S. Cater, P. Wady, T. Pirling, E. Jimenez-Melero, Residual stress distribution in friction stir welded ODS steel measured by neutron diffraction, J. Mater. Process. Technol. 246 (2017) 305–312, https://doi.org/10.1016/j.jmatprotec.2017.03.013.
[34] International (2023) E975–E1022, https://doi.org/10.1520/E0975-22.
[35] E.S. Rowland, S.R. Lyle, The application of Ms points to case depth measurement, Trans. Am. Soc. Met. 37 (1946) 27–47.
[36] S. Zenitani, N. Hayakawa, J. Yamamoto, K. Hiraoka, Y. Morikage, T. Kubo, K. Yasuda, K. Amano, Development of new low transformation temperature welding consumable to prevent cold cracking in high strength steel welds, Sci. Technol. Weld. Join. 12 (2007) 516–522, https://doi.org/10.1179/174329307X213675.
[37] Z. Feng, N. Ma, K. Hiraoka, Y. Komizo, S. Kano, M. Nagami, Development of 16Cr8Ni low transformation temperature welding material for optimal characteristics under various dilutions due to all repair welding positions, Sci. Technol. Weld. Join. 28 (2023) 305–313, https://doi.org/10.1080/13621718.2022.2158282.
[38] C.Y. Huo, H.L. Gao, Strain-induced martensitic transformation in fatigue crack tip zone for a high strength steel, Mater. Charact. 55 (2005) 12–18, https://doi.org/10.1016/j.matchar.2005.02.004.
[39] T. Zhang, Y. Wang, C. Zhang, L. Wang, H. Di, W. Xu, High cycle fatigue properties and fatigue crack propagation behavior of a bainite railway axle steel, Int. J. Fatigue 172 (2023) 107641, https://doi.org/10.1016/j.ijfatigue.2023.107641.